

## Perturbative High Harmonic Wave Front Control

Zhengyan Li,<sup>1,2\*</sup> Graham Brown,<sup>1,2</sup> Dong Hyuk Ko,<sup>1,2</sup> Fanqi Kong,<sup>1,2</sup> Ladan Arissian,<sup>1,2</sup> and P. B. Corkum<sup>1,2†</sup>

<sup>1</sup>Department of Physics, University of Ottawa, 25 Templeton St., Ottawa, ON, Canada K1N 6N5

<sup>2</sup>Joint Attosecond Science Laboratory, National Research Council and University of Ottawa,

100 Sussex Drive, Ottawa, Ontario, Canada K1A 0R6

(Received 15 April 2016; published 20 January 2017)

We pattern the wave front of a high harmonic beam by intersecting the intense driving laser pulse that generates the high harmonic with a weak control pulse. To illustrate the potential of wave-front control, we imprint a Fresnel zone plate pattern on a harmonic beam, causing the harmonics to focus and defocus. The quality of the focus that we achieve is measured using the spectral wave-front optical reconstruction by diffraction method. We will show that it is possible to enhance the peak intensity by orders of magnitude without a physical optical element in the path of the extreme ultraviolet (XUV) beam. Through perturbative wave-front control, XUV beams can be created with a flexibility approaching what technology allows for visible and infrared light.

DOI: 10.1103/PhysRevLett.118.033905

High harmonic generation is a nonperturbative nonlinear optical process [1], in contrast to conventional perturbative nonlinear optics [2]. The two realms can be bridged by a wave mixing process during high harmonic generation [3]. In this approach, a harmonic extreme ultraviolet (XUV) photon with frequency  $\Omega$  is a combination of  $l$  driving photons with frequency  $\omega_d$  and  $m$  perturbing photons with harmonic frequency  $\omega_p$  ( $\Omega = l\omega_d + m\omega_p$ ). The harmonic intensity scales as  $I_{\text{pert}}^m$ , where  $I_{\text{pert}}$  is the perturbing beam intensity. This scheme has led to advanced optical measurement techniques for isolated attosecond XUV pulses [4].

In contrast to optical characterization, spatiotemporal control of high-harmonic radiation remains challenging compared to visible light [5]. Conventionally, XUV focusing is achieved using glancing incident mirrors [6] and multilayer mirrors [7]. For a spatially coherent XUV beam such as high harmonics, physical Fresnel zone plates [8,9] have been used to focus a harmonic to microsize [9,10] or to select a single harmonic from a high harmonic spectrum [11]. All XUV optical components are demanding to manufacture.

We introduce a weak control beam to gently modify the high harmonic generation process. Similar to coherent control of a high harmonic spectrum [12] or of quantum dynamics [13,14], the interplay between two beams controls the electron recollision phase and, thus, imprints a controllable phase structure on the high-harmonic wave front while the XUV radiation is being generated. This perturbative control directly leads to all-optical XUV phase-modulation optics—effectively, a spatial light phase modulator for high harmonics.

Perturbative control of the high-harmonic wave front can be analyzed using the semiclassical model of high harmonic generation [1,15]. In this model, each harmonic emission is related to an electron trajectory characterized by

the canonical momentum  $k_0$ , the electron birth time  $t_b$ , and the recollision time  $t_c$ . All of these parameters are determined by the driving field  $E_d = E \cos(\omega_d t)$ . When a perturbative field  $E_p = \Delta E \cos(\omega_p t + \phi)$  is applied, the harmonic phase is related to the action of the corresponding electron trajectory. The phase variation due to the perturbative field is given by [15]

$$\delta\Phi_q = -\frac{E\Delta E}{\omega_d\omega_p} \int_{t_b}^{t_c} [\sin(\omega_d t_b) - \sin(\omega_d t)] \sin(\omega_p \tau + \phi) d\tau. \quad (1)$$

This harmonic phase shift can be calculated by determining  $k_0$ ,  $t_b$ , and  $t_c$  for harmonic  $q$  using the saddle point method [1]. With this method,  $t_b$  can have an imaginary part, representing the tunneling time. We define parameters  $C_q$  and  $\psi_q$  for harmonic  $q$  that are independent on perturbing field amplitude  $\Delta E$  and phase  $\phi$ .  $C_q = |-(E^2/\omega_d\omega_p) \times \int_{t_b}^{t_c} (\sin \omega_d t_b - \sin \omega_d t) \exp(i\omega_p \tau) d\tau|$  and  $\psi_q = \arg[-(E^2/\omega_d\omega_p) \int_{t_b}^{t_c} (\sin \omega_d t_b - \sin \omega_d t) \exp(i\omega_p \tau) d\tau] - \pi/2$ .  $\delta\Phi_q$  can be expressed as  $C_q \Delta E/E \cos(\phi + \psi_q)$ .

Thus, at the nonlinear medium, the near field harmonic radiation, carrying the phase modulation  $\delta\Phi_q$ , can be decomposed into terms according to harmonic wave-front modulation order  $m$

$$E_q \propto \exp(i\delta\Phi_q) = \exp\left(iC_q \frac{\Delta E}{E} \cos(\phi + \psi_q)\right) = \sum_{m=-\infty}^{\infty} i^m J_m(C_q \Delta E/E) e^{im(\phi + \psi_q)}, \quad (2)$$

where  $m$  is an integer and  $J_m$  is the  $m$ th order Bessel function. Each term  $E_q^{(m)} = i^m J_m(C_q \Delta E/E) e^{im(\phi + \psi_q)}$  describes how the perturbative wave-front phase  $\phi$  is

imprinted onto each harmonic. The modulation efficiency of the  $m$ th component of the  $q$ th harmonic beam is optimized when  $C_q \Delta E/E$  reaches the first maximum of  $|J_m|^2$ . If the harmonic phase modulation satisfies  $C_q \Delta E/E \ll 1$ , the  $m$  component of harmonic wave  $E_q^{(m)} \propto (\Delta E/E)^m$  satisfies the scaling law  $I_{\text{pert}}^m$  of harmonic intensity in Ref. [3].

To demonstrate perturbative control, we have constructed an all-optical Fresnel zone plate for XUV high harmonic radiation. As illustrated in Fig. 1, in the nonlinear medium, we use a driving laser field with a flat wave front, while the perturbing beam is incident at an oblique angle  $\theta$  and is tightly focused millimeters away from their intersection point. Thus, in the nonlinear medium, the perturbing field has a radius of curvature,  $R$  (positive for diverging field and negative for converging).  $|R|$  is significantly larger than the Rayleigh range of the tightly focused perturbing beam. Thus, it is controlled by varying the perturbing beam focal position relative to the gaseous nonlinear medium, and  $|R|$  approximately equals the distance between them.

The perturbation to the wave front of harmonic  $q$  is given by  $\delta\Phi_q = C_q \Delta E/E \cos[k_p(x^2 + y^2)/2R + k_p \theta y + \psi_q]$ , where  $k_p = 2\pi/\lambda_p$  is the wave vector of the perturbing beam and  $\lambda_p$  is its wavelength.  $\delta\Phi_q$  represents a concentric ring shaped phase modulation map. These rings are centered at  $(x_0, y_0) = (0, -R\theta)$  with ring radius  $r_n = \sqrt{n\lambda_p|R|}$  for the  $n$ th ring. A conventional phase zone plate has a similar concentric-ring structure [17], and the  $n$ th ring radius  $r_n$  follows the same  $r_n \propto \sqrt{n}$  relation. Therefore, each harmonic  $q$  has a phase pattern  $\delta\Phi_q$  imprinted on its spatial profile that is essentially equivalent to the pattern

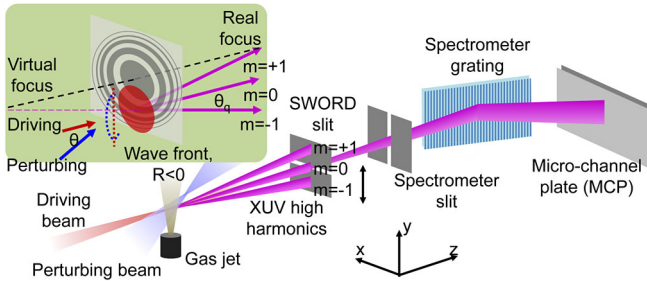


FIG. 1. Schematic diagram of experimental setup. The inset shows details in the nonlinear gas medium. In the case illustrated in the figure (converging perturbing field with  $R < 0$ ), high harmonics are generated in the red circle area, covering the bottom part of the multiring zone plate pattern which is constructed by interference between the loosely focused 800 nm driving and tightly focused 400 nm perturbing beams. The  $m = 1$  components of harmonics converge to the zone plate real foci, and the  $m = -1$  components diverge from virtual foci. The SWORD (spectral wave-front optical reconstruction by diffraction) slit is used for measuring the one-dimensional ( $y$ ) lineout of the XUV wave front [16].

created by a zone plate placed at the exit of the gas medium where the harmonics are generated.

We consider the case where  $\omega_p = 2\omega_d$ . Neighboring attosecond pulses in the train that makes the high harmonic radiation have a time delay of a half cycle of the driving field, and  $\phi$ , the relative phase difference between the driving field and the perturbing field, has  $\pi$  shift. So, phase perturbations of these neighboring attosecond pulses are  $\delta\Phi_q$  and  $-\delta\Phi_q$ , respectively, according to Eq. (1). The effective field of even harmonic  $q$  sums these neighboring attosecond pulses and is proportional to  $e^{i\delta\Phi_q} - e^{-i\delta\Phi_q} \propto \sin[C_q \Delta E/E \cos(\phi + \psi_q)]$ . Thus, it is the amplitude of the even harmonic that is modulated in this case, and therefore, the wave front gains the characteristics of passing through a transmission zone plate.

For any  $m$  component, due to the opposite phase shift of the neighboring attosecond pulses, the effective field of harmonic  $q$  is proportional to  $e^{i\delta\Phi_q} - (-1)^q e^{-i\delta\Phi_q} = \sum_{m=-\infty}^{\infty} [1 - (-1)^{m+q}] i^m J_m(C_q \Delta E/E) e^{im(\phi + \psi_q)}$  according to Eq. (2). Thus, modulation of harmonics is only available when  $m + q$  is odd. This is equivalent to the parity conservation condition in harmonic wave mixing [3]. In our experiment, the driving laser wavelength is 800 nm and the perturbing wavelength is 400 nm. For  $m = \pm 1$ , only even order harmonics are modulated.

The modulation depth of the harmonic phase is controlled by the perturbing intensity. In the experiment, the perturbing intensity is 3 orders of magnitude smaller than the driving beam intensity ( $2 \times 10^{14}$  W/cm<sup>2</sup>, determined by the high harmonic cutoff energy). For example, when  $(\Delta E/E)^2 = 5 \times 10^{-3}$ , numerical calculation of Eq. (1) showed that the maximum harmonic phase modulation that occurs for  $\delta\Phi_q$  is approximately  $0.3\pi$ . When the intensity ratio increases to  $\sim 2 \times 10^{-2}$ , the energy of  $m = \pm 1$  components of the harmonic beam is optimized with  $\delta\Phi_q = 0.58\pi$ .

Analogous to a physical zone plate [17], the principle focal spot for harmonic  $q$  is real and located

$$f_q = qR\lambda_p/\lambda_d, \quad (3)$$

after the gas medium ( $\lambda_d$  driving beam wavelength), while a conjugate virtual focus is  $f_q$  before the medium. The focal spot size scales as  $\lambda_d f_q/qD = \lambda_p R/D$  where  $D$  is the harmonic beam size at the gas medium. The lower limit of a first-order zone-plate focus is the perturbing beam focus. Higher-order foci are available at  $\pm f_q/|m|$  (“+” for real foci and “-” for virtual foci). They have focal spot diameters that are  $|m|$  times smaller than the first-order foci but require stronger perturbing fields to maximize  $|J_m|^2$ . Based on Eq. (3), a shorter perturbing field wavelength also leads to a shorter zone plate focal length and a tighter focus.

In the transverse direction, the noncollinear perturbing geometry [18,19] shifts the zone plate foci away from the driving beam axis by  $\Delta y = -R\theta$ . Thus, for practical

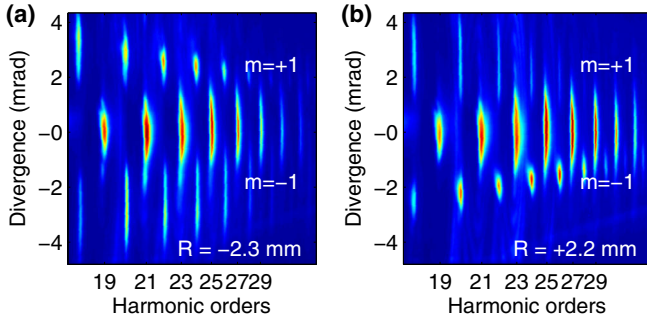


FIG. 2. Far field divergence measurement of high harmonic spectra including the  $m = \pm 1$  components and the undeflected ( $m = 0$ ) harmonic beam when (a)  $R = -2.3$  mm, and (b)  $R = 2.2$  mm. The nonlinear gas medium is placed 5 mm before the driving laser focus.

application, material damage by the driving laser field is avoided due to the oblique perturbative angle  $\theta$ . However, the noncollinear geometry is not, otherwise, necessary.

Now, we turn to experimental results for short trajectory harmonics (the long trajectory signal is considerably weaker). We begin by using our spectrometer for a direct, but qualitative, measurement of the beams [without the spectral wave-front optical reconstruction by diffraction (SWORD) slit in Fig. 1]. The spectrometer spreads the harmonics along the horizontal ( $x$ ) direction while the other ( $y$ ) direction records their divergence.

In our first demonstration, we place the gas jet 5 mm before the driving beam focus, so the unperturbed harmonic beam diverges due to the transverse intensity gradient of the driving beam [20,21]. Our aim is to partially correct this divergence. Figures 2(a) and 2(b) shows the high harmonic spectrum when the perturbing wave-front curvature at the medium is  $R = -2.3$  mm (the perturbing beam has a converging wave front at the jet) and 2.2 mm (diverging wave front), respectively. We use the  $m = \pm 1$  terms of the harmonic radiation.

The  $m = 1$  components (even harmonics) propagate towards the  $y > 0$  direction with the angle  $\theta_{\lambda_d}/q\lambda_p$ . When the perturbative field is converging ( $R < 0$ ), the  $m = 1$  harmonic beams are focused closer to the detector and the beam size decreases [Fig. 2(a)]. In contrast, when we have a diverging perturbing field ( $R > 0$ ), the  $m = 1$  harmonic beams are defocused, exaggerating the beam divergence [Fig. 2(b)]. For the  $m = -1$  components, the near field harmonic phase is inverted, so their propagation angles are  $-\theta_{\lambda_d}/q\lambda_p$  along  $y < 0$ . The  $m = -1$  harmonic beams are diverged with  $R < 0$  and focused with  $R > 0$ . These coexisting focused and defocused harmonic beams are related to the real and virtual zone plate foci, respectively.

For a more precise characterization of the wave-front curvature and zone plate foci, we turn to SWORD [16]. SWORD is analogous to a one-dimensional spectrally resolved Shack-Hartmann wave-front sensor [22]. In

Fig. 1, the 25  $\mu\text{m}$  SWORD slit moves along the vertical ( $y$ ) direction with 20  $\mu\text{m}$  steps. 20  $\mu\text{m}$  is small compared to the few hundred micron beam size. The spectrometer slit selects a vertical lineout of the SWORD slit-diffracted beam, yielding a frequency-resolved diffraction pattern at the detector. By determining the position of the central fringe of the diffraction pattern, we determine the wave-front gradient of harmonic  $q$  at position  $y$ , equivalent to spatial phase distribution  $\phi_q(y)$ . The total energy contained in the diffraction pattern leads to the intensity distribution  $I_q(y)$ . Once amplitude (solid lines) and phase (dashed lines) are known at the slit ( $z = 0$ ), the beam is fully characterized [Fig. 3(a) for harmonic 22 (H22)]. It can be projected everywhere in space.

We reconstruct the even harmonics field distribution at any location before the SWORD slit by propagating the field  $E_q(y, z = 0) = \sqrt{I_q(y)} \exp[i\phi_q(y)]$  back toward the gas medium using the one-direction wave propagation equation  $\partial_z E_q(y, z) = i\lambda_d/(4\pi q)\partial_{yy} E_q(y, z)$  [23]. In this

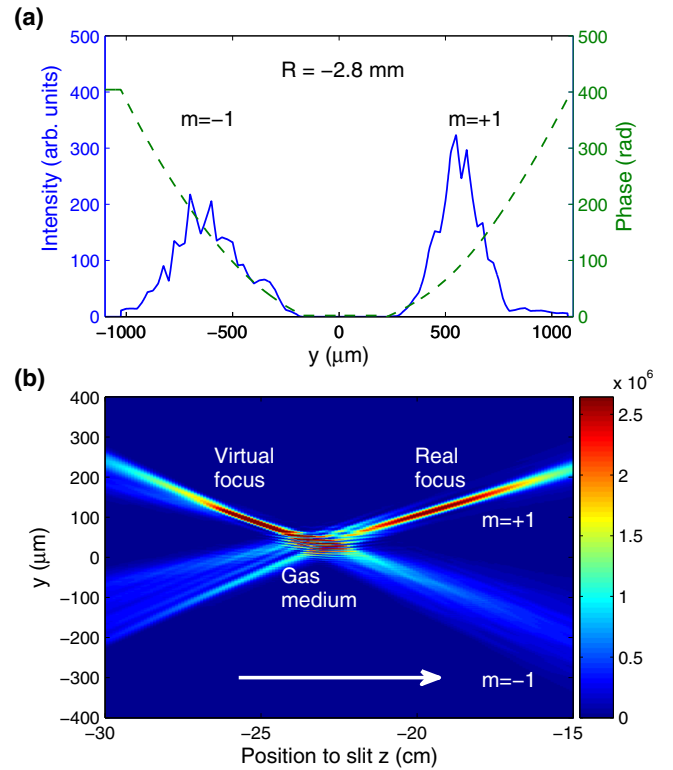


FIG. 3. SWORD measurement of the  $m = \pm 1$  components of H22 radiation. (a) Measured intensity (solid line) and phase (dashed line) distribution along  $y$  or vertical direction of the  $m = 1$  (right) and  $m = -1$  (left) components of H22 radiation at the SWORD slit ( $z = 0$ ). The perturbing wave-front radius of curvature is  $R = -2.8$  mm. (b) Intensity  $y$  distribution of XUV field at  $z$  positions before the SWORD slit, reconstructed from XUV field at the slit in (a) through backpropagation. The nonlinear gas medium is placed 10 mm before the driving laser focus. The arrow shows the propagation direction of laser and harmonic beams.



way, we locate the beam foci by searching for the  $z$  position maximizing  $|E_q(y, z)|^2$  and obtain the transverse  $y$  profile of the focal spots.

The H22 intensity distribution along the  $y$  (or vertical) direction is shown as a function of distance from the SWORD slit in Fig. 3(b) where we have used a perturbing beam with a concave wave front ( $R = -2.8$  mm). In the figure, the beam propagates to the right as illustrated by the arrow in the figure. The measurement shows that the  $m = \pm 1$  component of H22 cross at 23 cm before the SWORD slit. This is the exact position where we have placed the gas medium.

For this aspect of the experiment, we have placed the gas jet 10 mm before the driving beam focus to minimize the intensity gradient effect. In this configuration, the focal positions and sizes are predominantly determined by the zone plate. There are two foci in Fig. 3(b). The  $m = 1$  and  $-1$  components have their intensity maximum and the smallest transverse size at 20 and 25 cm before the SWORD slit, respectively, corresponding to the real and virtual foci of the zone plate for H22. For the  $m = 1$  component, the focal length is  $3.4 \pm 0.6$  cm. This is the distance between the real focus and the crossing point of the  $m = \pm 1$  harmonic beams. The full width at half maximum (FWHM) size of the real focus is  $16 \pm 1 \mu\text{m}$ , approximately one third the beam size at the gas medium ( $50 \pm 10 \mu\text{m}$ ).

The  $m = -1$  virtual focus is closer to the gas medium than its counterpart real focus because of a small remaining divergence imprinted on the XUV by the intensity gradient of the driving beam [20,21]. Next, we quantitatively compare our zone plate foci characterization results with simulations including such complexities.

We use the strong field approximation [1], and propagate the  $m = \pm 1$  harmonic beams to calculate the real focal positions and spot sizes. As shown in Fig. 4(a), for both simulation (solid line) and experiment (circles), the real focal lengths of the H22 beams, either  $m = 1$  components for  $R < 0$  or  $m = -1$  components for  $R > 0$ , agree within error. Both decrease as  $|R|$  decreases, as discussed in Eq. (3).

The focal spot sizes also decrease as  $|R|$  decreases [Fig. 4(b)], reflecting the fact that the focal length, or  $f$  number, decreases. The minimum FWHM focal size that we measured is  $13 \pm 1 \mu\text{m}$  when  $R = 1.2$  mm. This is approximately one fourth the beam size at the gas medium ( $50 \pm 10 \mu\text{m}$ ). If the second harmonic intensity were appropriately chosen, we might expect  $\sim |J_{\pm 1}(0.58\pi)|^2 = 34\%$  energy of the radiation to be deflected into the  $m = \pm 1$  component beams. Meanwhile, the estimated pulse duration broadening of the focused harmonic pulse is negligible ( $< 2$  fs). Thus, an intensity enhancement of  $\sim 5$  times is available. However, the measured focal size is larger than the simulation prediction as  $|R|$  approaches 1 mm. We believe the difference is due to aberration on the

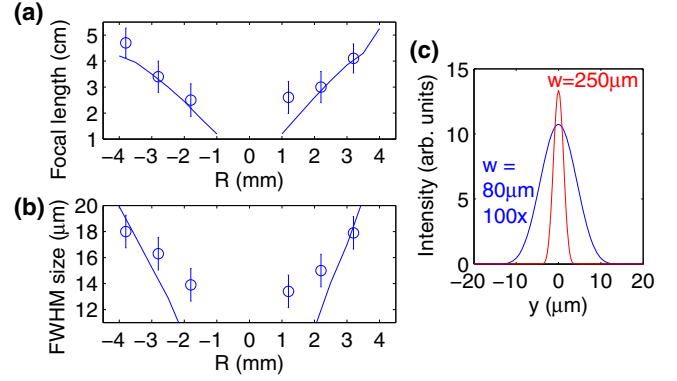


FIG. 4. Simulation of H22 zone plate foci and comparison with experiments. (a) Experimental (circle) and simulation (solid lines) results of real focal length. (b) Experimental (circle) and simulation (solid lines) results of real focal spot size. Both (a) and (b) are plotted as a function of the radius of curvature of the control beam wave front,  $R$ . (c) The intensity spatial profiles of focused H22 beams generated by narrow driving beam (blue line,  $1/e^2$  size  $w = 80 \mu\text{m}$ ) and wide driving beam (red line,  $1/e^2$  size  $w = 250 \mu\text{m}$ ) with the medium placed 10 mm before the driving beam focus. The driving beam intensities and other parameters for these two cases are the same (except the beam size), and the perturbing wave-front curvature is  $R = -2$  mm. The narrow driving beam ( $w = 80 \mu\text{m}$ ) induced H22 intensity is artificially multiplied by 100 times for comparison with the wide driving beam case ( $w = 250 \mu\text{m}$ ).

perturbing beam as the fundamental beam overlaps almost all of the perturbing beam near its focus.

In Figure 4(c), we show results of a simulation for a larger driving beam. For comparison, we use the same driving beam intensity and  $R = -2$  mm as the experiment, but increase the driving beam size ( $1/e^2$ ) from 80 to 250  $\mu\text{m}$ . The simulation shows that the H22 focal spot size shrinks from 10 to 2.9  $\mu\text{m}$  [Fig. 4(b)]. The peak intensity enhancement would be correspondingly larger by a further factor of 100 (10 from the higher energy beam created by the fundamental and another factor of 10 from the smaller focal spot). We anticipate that the focal spot size can reach submicrometer size and the intensity enhancement of 4–6 orders of magnitude seems feasible.

Before concluding, a reader may find it useful to link the wave-front description that we have used to the photon momentum. In momentum language, a net-single photon from the perturbing beam contributes to each photon of high harmonic emission ( $m = 1$ ) when  $R < 0$  in Fig. 1 [3]. Its momentum simultaneously focuses and deflects the harmonic, corresponding to the real zone plate focus. For the  $-1$  order, a net-single photon is emitted into the perturbing beam ( $m = -1$ ) and its momentum contributes to defocusing and deflection in the opposite direction [Fig. 2(a)]. Higher order diffraction (not shown) corresponds to net-2 ( $|m| = 2$ ) or more ( $|m| > 2$ ) photons absorbed from or emitted to the perturbing beam. However, while the photon momentum picture is

qualitatively useful, it is difficult to use for quantitative predictions.

In conclusion, we have introduced the concept of perturbative control for all-optical XUV optics and demonstrated it by controlling the wave-front curvature. Since control is exercised with a much smaller field than the driving field, the ionization process during high harmonic generation is not significantly impacted, and the accumulated harmonic wave-front phase  $\delta\Phi_q$  is proportional  $\Delta E/E$ . Intuitively, perturbative control is similar to the wave-mixing picture in conventional perturbative nonlinear optics [2], but the power law dependence of the modulated harmonic intensity to  $I_{\text{pert}}^m$  is not necessary for optimal zone plate formation.

One can take advantage of the general properties of perturbative control to construct different versatile all-optical XUV optics and actively tune their parameters or optical properties in a flexible way. For example, an XUV beam carrying tunable orbital angular momentum can be obtained [24].

Moreover, the wave-front control that we have proposed and demonstrated has several advantages. First, it deflects the focused XUV beam out of the path of the fundamental pulse. Thus, a sample can be placed at the XUV focus without risking damage from the high intensity fundamental. This could be important for femtosecond XUV pump-XUV probe experiments [25]. Second, an XUV monochromator can be constructed by translating a microdiameter pinhole along the central axis of the zone plate. Thus, the focused harmonic order is selected with limited temporal broadening and minimum energy loss [26,27]. Third, a zone plate produces the same focal spot size for each harmonic, making intensity comparisons between different harmonics more accurate. Finally, all-optical zone plates can be used to prefocus beams for further focusing with physical zone plates. This will allow even smaller foci (10 nm seems feasible) and allow many orders of magnitude intensity enhancement over what is currently available [28].

We acknowledge important financial support from the U.S. Defense Advanced Research Projects Agency PULSE Program, from Aviation and Missile Research, Development, and Engineering Center (Grant No. W31P4Q1310017), and the U.S. Air Force Office of Scientific Research (Grant No. FA9550-16-1-0109); The Canadian Canada Research Chairs Program, Natural Sciences and Engineering Research Council of Canada, the Canada Foundation for Innovation, and the Ontario Research Fund. We also acknowledge invaluable assistance from T. Clancy, Chunmei Zhang, and T. J. Hammond.

\*z128@uottawa.ca

†pcorkum@uottawa.ca

[1] M. Lewenstein, P. Balcou, M. Y. Ivanov, A. L'Huillier, and P. B. Corkum, *Phys. Rev. A* **49**, 2117 (1994).

- [2] R. W. Boyd, *Nonlinear Optics*, 3rd ed. (Academic, New York, 2008).
- [3] J. B. Bertrand, H. J. Wörner, H.-C. Bandulet, É. Bisson, M. Spanner, J.-C. Kieffer, D. M. Villeneuve, and P. B. Corkum, *Phys. Rev. Lett.* **106**, 023001 (2011).
- [4] K. T. Kim, C. Zhang, A. D. Shiner, S. E. Kirkwood, E. Frumker, G. Gariepy, A. Naumov, D. M. Villeneuve, and P. B. Corkum, *Nat. Phys.* **9**, 159 (2013).
- [5] J. A. R. Samson and D. L. Ederer, *Vacuum Ultraviolet Spectroscopy* (Academic, New York, 1998), Vol. I and II.
- [6] P. Kirkpatrick and A. V. Baez, *J. Opt. Soc. Am.* **38**, 766 (1948).
- [7] J. H. Underwood and T. W. Barbee, *Nature (London)* **294**, 429 (1981).
- [8] J. Kirz, *J. Opt. Soc. Am.* **64**, 301 (1974).
- [9] M. Schnürer, Z. Cheng, M. Hentschel, F. Krausz, T. Wilhein, D. Hambach, G. Schmahl, M. Drescher, Y. Lim, and U. Heinzmann, *Appl. Phys. B* **70**, S227 (2000).
- [10] H. Mashiko, A. Suda, K. Midorikawa, and K. Omi, in *Technical digest CD-ROM: CLEO/IQEC/PhAST Conference: San Francisco, 2004* (Optical Society of America, Washington, D.C., 2004), paper JMD1.
- [11] J. Metje *et al.*, *Opt. Express* **22**, 10747 (2014).
- [12] C. Winterfeldt, C. Spielmann, and G. Gerber, *Rev. Mod. Phys.* **80**, 117 (2008).
- [13] C. Brif, R. Chakrabarti, and H. Rabitz, *New J. Phys.* **12**, 075008 (2010).
- [14] T. Hornung, R. Meier, R. de Vivie-Riedle, and M. Motzkus, *Chem. Phys.* **267**, 261 (2001).
- [15] N. Dudovich, O. Smirnova, J. Levesque, Y. Mairesse, M. Yu. Ivanov, D. M. Villeneuve, and P. B. Corkum, *Nat. Phys.* **2**, 781 (2006).
- [16] E. Frumker, G. G. Paulus, H. Niikura, D. M. Villeneuve, and P. B. Corkum, *Opt. Lett.* **34**, 3026 (2009).
- [17] J. W. Goodman, *Introduction to Fourier Optics*, 3rd ed. (Roberts and Company Publishers, Englewood, CO, 2005).
- [18] C. M. Heyl, P. Rudawski, F. Brizuela, S. N. Bengtsson, J. Mauritsson, and A. L'Huillier, *Phys. Rev. Lett.* **112**, 143902 (2014).
- [19] D. D. Hickstein *et al.*, *Nat. Photonics* **9**, 743 (2015).
- [20] P. Salières, A. L'Huillier, and M. Lewenstein, *Phys. Rev. Lett.* **74**, 3776 (1995).
- [21] P. Balcou, P. Salières, A. L'Huillier, and M. Lewenstein, *Phys. Rev. A* **55**, 3204 (1997).
- [22] B. C. Platt and R. Shack, *J. Refract. Surg.* **17**, S573 (2001).
- [23] E. Frumker, G. G. Paulus, H. Niikura, A. Naumov, D. M. Villeneuve, and P. B. Corkum, *Opt. Express* **20**, 13870 (2012).
- [24] G. Gariepy, J. Leach, K. T. Kim, T. J. Hammond, E. Frumker, R. W. Boyd, and P. B. Corkum, *Phys. Rev. Lett.* **113**, 153901 (2014).
- [25] P. Tzallas, E. Skantzakis, L. A. A. Nikolopoulos, G. D. Tsakiris, and D. Charalambidis, *Nat. Phys.* **7**, 781 (2011).
- [26] P. Villorosi, *Appl. Opt.* **38**, 6040 (1999).
- [27] F. Frassetto, C. Cacho, C. A. Froud, I. C. Edmund Turcu, P. Villorosi, W. A. Bryan, E. Springate, and L. Poletto, *Opt. Express* **19**, 19169 (2011).
- [28] W. Chao, P. Fischer, T. Tylliszczak, S. Rekawa, E. Anderson, and P. Naulleau, *Opt. Express* **20**, 9777 (2012).